

# Autonomous landing of underwater vehicles using mm-resolution laser bathymetry

Mehul Sangekar, *Member, IEEE*, Blair Thornton, *Member, IEEE*, Adrian Bodenmann, *Member, IEEE*, and Tamaki Ura, *Life Fellow, IEEE*

## Abstract

This paper describes a framework for an autonomous underwater vehicle to safely land on the seafloor. The design of an underwater vehicle with mm-resolution mapping system using structured light and hardware suitable for landing is proposed. A landing algorithm has been developed which uses this mm-resolution bathymetry to detect landing area on the seafloor. The algorithm identifies candidate sites within the landing area where an underwater vehicle of known geometry can safely land to make further observations or perform tasks on the seafloor. The algorithm also selects between multiple candidate sites based on a cost function that identifies the most suitable site for landing. To evaluate its performance, the algorithm was implemented on seafloor bathymetry obtained using an AUV with an equivalent high resolution mapping system during a real underwater survey at a seamount.

## Index Terms

Autonomous landing, Seafloor observations, Seafloor mapping, Structured light, Autonomous Underwater Vehicle

M. Sangekar is a project researcher with the Institute of Industrial Science, The University of Tokyo (email: mehul@iis.u-tokyo.ac.jp)

B. Thornton is an Associate Professor at the Southampton Marine and Maritime Institute, University of Southampton with an adjunct cross appointment at the Institute of Industrial Science, The University of Tokyo (email: b.thornton@soton.ac.uk)

A. Bodenmann is a project researcher with the Institute of Industrial Science, The University of Tokyo (email: adrian@iis.u-tokyo.ac.jp)

T. Ura is associated with the Center for Socio-Robotic Synthesis, Kyushu Institute of Technology (email: ura@lsse.kyutech.ac.jp)

This work was supported by the Japanese Ministry of Education under the Program for the "Development of Fundamental Tools for the Utilization of Marine Resources".

18

## I. INTRODUCTION

19 The use of unmanned underwater vehicles for exploration of mineral deposits [1], such as  
20 manganese crusts [2], manganese nodules [3] and seafloor massive sulfides [4] has gained mo-  
21 mentum in recent years. While high resolution bathymetric maps of the seafloor generated using  
22 acoustic [5] or visual [6] mapping systems are useful for recognizing visible and morphological  
23 seafloor features [7][8], measurement of chemical composition [9] or frictional coefficient [10] of  
24 seafloor deposits require direct contact for obtaining measurements. There have been significant  
25 developments over the past decade that provide in-situ methods to make measurements of  
26 the chemical and geological properties of the seafloor, such as underwater microscopy [11],  
27 gamma radiation measurements [12][13], laser induced breakdown spectroscopy (LIBS) [14][15],  
28 laser Raman spectroscopy [16][17] and seafloor stiffness and frictional coefficients [18]. The  
29 development of these new classes of analytical sensors that requires direct contact motivates  
30 the development of landing capabilities for Autonomous Underwater Vehicles (AUVs) to deliver  
31 these abilities in a more scalable manner. Underwater terrain in regions such as those with  
32 mineral deposits can change abruptly and vary at short intervals on spatial scales that cannot  
33 be observed from the surface. Therefore the reliable use of in-situ instruments such as those  
34 described, and the safety of the underwater vehicle requires real-time detection of safe landing  
35 sites. Although ROV pilots can identify safe landing sites to achieve the proximity needed to  
36 perform in-situ chemical measurements with the instrument, at present AUVs lack this capability.

37 In this research, we developed a framework to enable an underwater vehicle land on the seafloor  
38 autonomously by identifying safe landing sites in real-time. The design of an underwater vehicle  
39 was proposed by identifying hardware suitable for landing on the seafloor. A mm-resolution  
40 mapping system using structured light was also implemented as part of the vehicle design. The  
41 conditions for safe landing were identified to develop an algorithm which uses this mm-resolution  
42 seafloor bathymetry to identify landing area on the seafloor and an exclusion zone where the  
43 centre of gravity is prohibited from landing. Within this landing area, the algorithm detects safe  
44 landing sites along different landing headings where an underwater vehicle of a given geometry  
45 can fit. The algorithm selects the final landing site from the candidates using a cost function that  
46 takes into account properties of the seafloor terrain at the sites. The algorithm was implemented  
47 on over 1000 sq.m. of seafloor bathymetry obtained by an AUV with an equivalent mapping  
48 system at the No.5 Takuyo seamount in the Northwest-Pacific to evaluate its performance. The

49 results are analyzed to demonstrate the feasibility of using the landing framework in real seafloor  
50 surveys.

51 The remainder of this paper is organized as follows; section II discusses the challenges  
52 associated with autonomous landing of an underwater vehicle along with previous research in this  
53 field. Section II describes the proposed design of an underwater vehicle capable of landing. The  
54 high resolution mapping system for generating bathymetry with mm-resolution is also described.  
55 In Section III, the different steps of the algorithm to identify landing sites are described and  
56 demonstrated by simulating its performance on seafloor data obtained using an equivalent high  
57 resolution mapping system. Section IV describes the implementation of the algorithm on seafloor  
58 bathymetry obtained using an AUV during a real underwater survey, the results of which are  
59 also published. Section V provides conclusion to this work.

60 **II. PROBLEM FORMULATION**

61 The detailed topography of the seafloor relevant for landing of underwater vehicles can be  
62 rough and vary abruptly on scales that are too small to be captured by traditional ship based  
63 acoustic multibeam systems. Seafloor in areas of interest can have complex and abruptly varying  
64 terrains, as seen in Fig. 1 which illustrates scenes from a manganese crust survey at No.5 Takuyo  
65 seamount [19].

66 These prohibit landing simply at random locations and requires intelligent choice of landing  
67 sites. However, the large localization uncertainty [20] associated with deep sea operations means  
68 that landing sites determined prior to deployment cannot be reached with sufficient navigational  
69 accuracy. Therefore, the AUV should have capability to identify landing sites during the survey.  
70 This requires it to be equipped with a mapping system capable of generating bathymetry with  
71 sufficiently high resolution, such as those based on light sectioning [21] [22]. While landing site  
72 detection for aerial vehicles has been previously demonstrated in [23] [24], conditions essential  
73 for safe landing with a stable footing in underwater environments need to be investigated.  
74 Simulations for control, navigation and dynamics of AUVs with landing capabilities have been  
75 reported in [25][26]. However, these previous works do not develop the intelligence necessary for  
76 an AUV to identify areas where it can land safely. This identifies need for an algorithm to perform  
77 real-time analysis of seafloor bathymetry to detect landing sites based on the terrain and geometry  
78 of the AUV. The use of Fourier analysis for seafloor terrain segmentation and 3D alignment in  
79 post-survey processing has been previously demonstrated in [27][28]. Other methods for surface

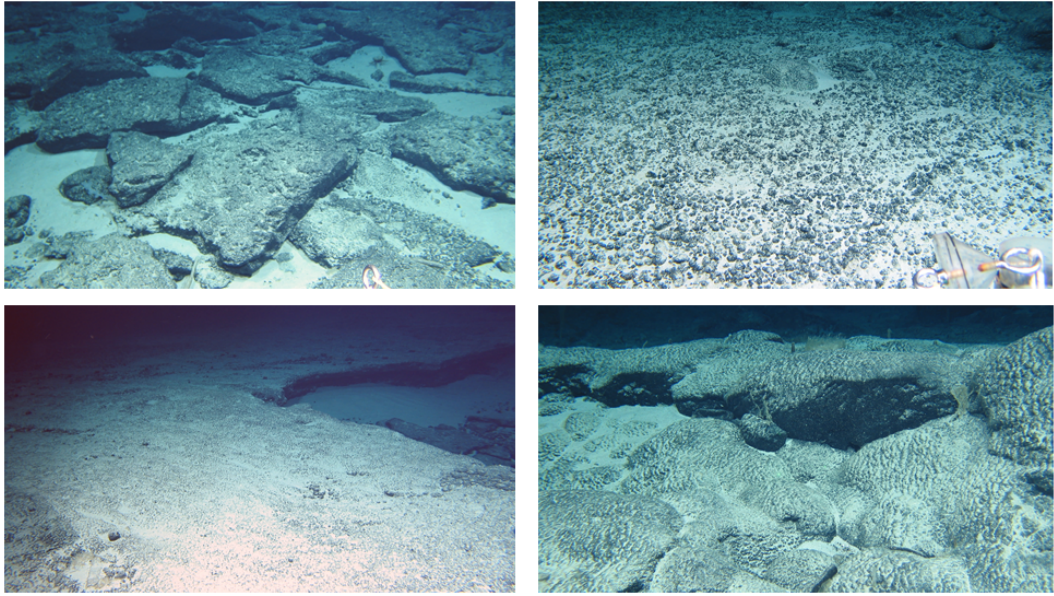


Fig. 1. Different seafloor terrain at No.5 Takuyo seamount. Clockwise, from top left: Broken slabs in sand, nodules, pillowy crusts and continuous flat crusts

80 classification using wavelets [29] have also been demonstrated before but have not been applied  
 81 earlier to landing site identification. Early works by our group demonstrated a landing algorithm  
 82 using Fourier analysis to separate flat ground surface from objects on the seafloor [30]. The  
 83 algorithm rejected all objects as non-landing areas without analyzing the possibility of landing  
 84 on objects depending on their size. Also, only extremely flat areas were considered for landing  
 85 and detailed analysis of landing on slopes was not performed. This work builds on our previous  
 86 work and develops a complete comprehensive framework for landing including the a design of  
 87 an underwater vehicle.

88

### III. UNDERWATER LANDING VEHICLE

89 The design of an underwater vehicle was made after taking into consideration essential  
 90 hardware for landing on the seafloor. In this work, we propose the developed of an underwater  
 91 vehicle with negative buoyancy for landing. The negative buoyancy allows the AUV to land  
 92 with minimum use of vertical thrust and remain stationary after landing while making seafloor  
 93 observations. This also saves power and provides a vibration free environment for sensors.

94 A. Vehicle hardware

95 The design features on the vehicle can be seen in the Fig. 2. Two horizontal thrusters provide  
 96 surge and heading control while two thrusters, inclined at  $22.5^\circ$  with the vertical, control sway  
 97 and heave. Independent heave, surge, sway and heading control allows the vehicle to perform  
 98 slow speed manoeuvres and hover when necessary. The inclined thrusters also direct the thrust  
 99 away from the area directly below the vehicle minimizing the disturbance of sand and sediments  
 100 during landing.

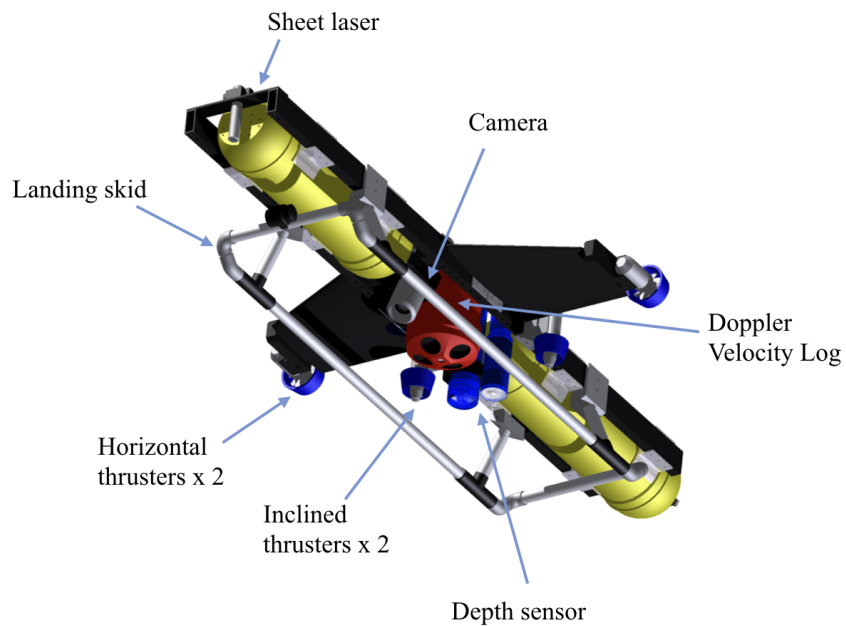


Fig. 2. Hardware features on the the underwater vehicle

101 The vehicle is designed to be negatively buoyant for landing. Although variable buoyancy  
 102 engines are available [31], for our vehicle, negative buoyancy was obtained using fixed weights.  
 103 A NACA651412 wing profile is used to offset the negative buoyancy by generating lift during  
 104 forward motion at zero angle of attack. A nylon landing skid provides stable footing and protects  
 105 sensors under the vehicle. Navigation is performed using dead reckoning by integrating the  
 106 velocity obtained from a Doppler Velocity Log (DVL) and orientation with a pressure depth  
 107 sensor to estimate the state of the vehicle at any moment in time. Although during landing, the  
 108 vehicle can use altitude measurements from DVL beam range to estimate its distance from the  
 109 seafloor, these fail to work below 0.3 m range. We propose to use record the depth of the vehicle  
 110 before landing from an altitude of 1 m and estimate the depth at the landing point.

111 *B. High resolution mapping system*

112 A high resolution mapping system [32] using light sectioning is integrated into the vehicle  
 113 for generating mm-resolution bathymetry. The hardware components of the system can be seen  
 114 in Fig. 3 and the parameters associated are explained in the Table I. The system uses a sheet  
 115 laser which projects a laser on the seafloor whose projection is captured by a camera mounted  
 116 at an angle. The pixels in the image belonging to the laser image are identified and converted to  
 117 local coordinates using the geometry of the system. These are then converted to earth coordinates  
 118 using the position of the vehicle.

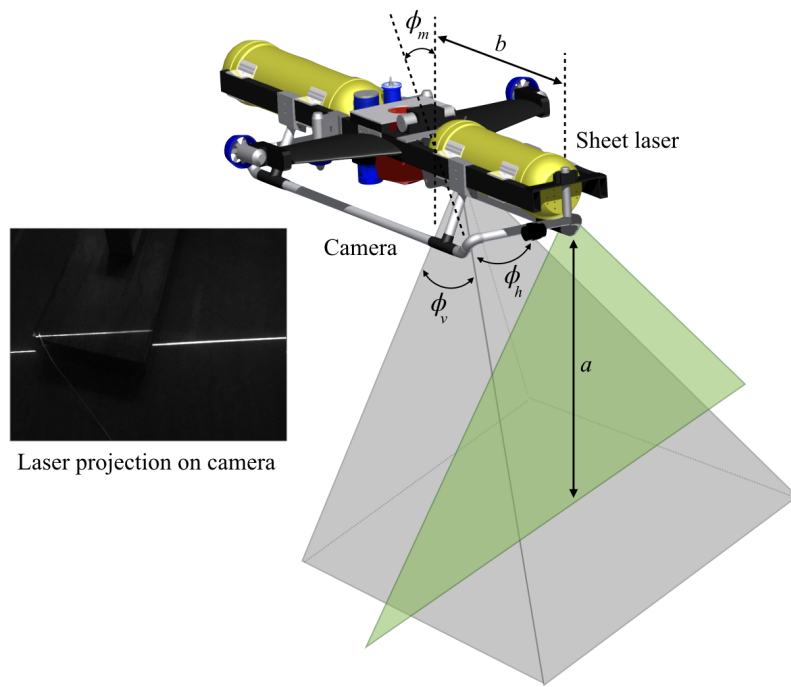


Fig. 3. Setup and working of the high resolution mapping system

TABLE I  
PARAMETERS OF THE MAPPING SYSTEM

Property	Value
Mapping altitude	$a$
Baseline between camera and laser	$b$
Vertical mounting angle of camera	$\phi_m$
Horizontal opening angle of camera	$\phi_h$
Vertical opening angle of camera	$\phi_v$

119

#### IV. AUTONOMOUS LANDING ALGORITHM

120 The processing pipeline of the algorithm can be broken down into the following main steps.

121 1) *Data preprocessing*: The algorithm uses high resolution point cloud generated from a  
122 mapping system as input. The preprocessing step brings the point cloud into a uniform resolution  
123 for analysis.

124 2) *Landing area detection*: The conditions for safe landing on the seafloor are identified for  
125 detecting a safe landing area within the point cloud. An exclusion zone is also identified where  
126 the centre of gravity of the vehicle is prohibited from landing.

127 3) *Landing site identification*: Within the detected landing area, landing sites are identified  
128 which are regions where an AUV of a particular geometry can fit along a certain heading.  
129 Landing site properties are extracted for all the identified sites along different headings.

130 4) *Final landing site selection*: Landing costs are calculated for all the sites using the landing  
131 site properties. The site with minimum landing cost is finally selected as the final landing site.

132 *A. Data preprocessing*

133 The algorithm requires high resolution bathymetry point cloud generated from a mapping  
134 system as described in Section III-B. Data was collected at a Manganese crust site on the No.5  
135 Takuyo seamount by a similar mapping system mounted on the AUV BOSS-A during KR16-01  
136 cruise of R/V Keirei, the specifications of which are given in Table. II. Fig. 4a shows a 25 m  
137 section of the bathymetry point cloud mapped at an heading of  $-130^\circ$

TABLE II  
PROPERTIES OF THE MAPPING SYSTEM

Property	Value
Mapping altitude $a$	2 m
Baseline between camera and laser $b$	1.025 m
Vertical mounting angle of camera $\phi_m$	$70^\circ$
Horizontal opening angle of camera $\phi_h$	$60.2^\circ$
Vertical opening angle of camera $\phi_v$	$50.4^\circ$
Along-track resolution	4 mm
Cross-track resolution	3 mm
Vertical resolution	6 mm

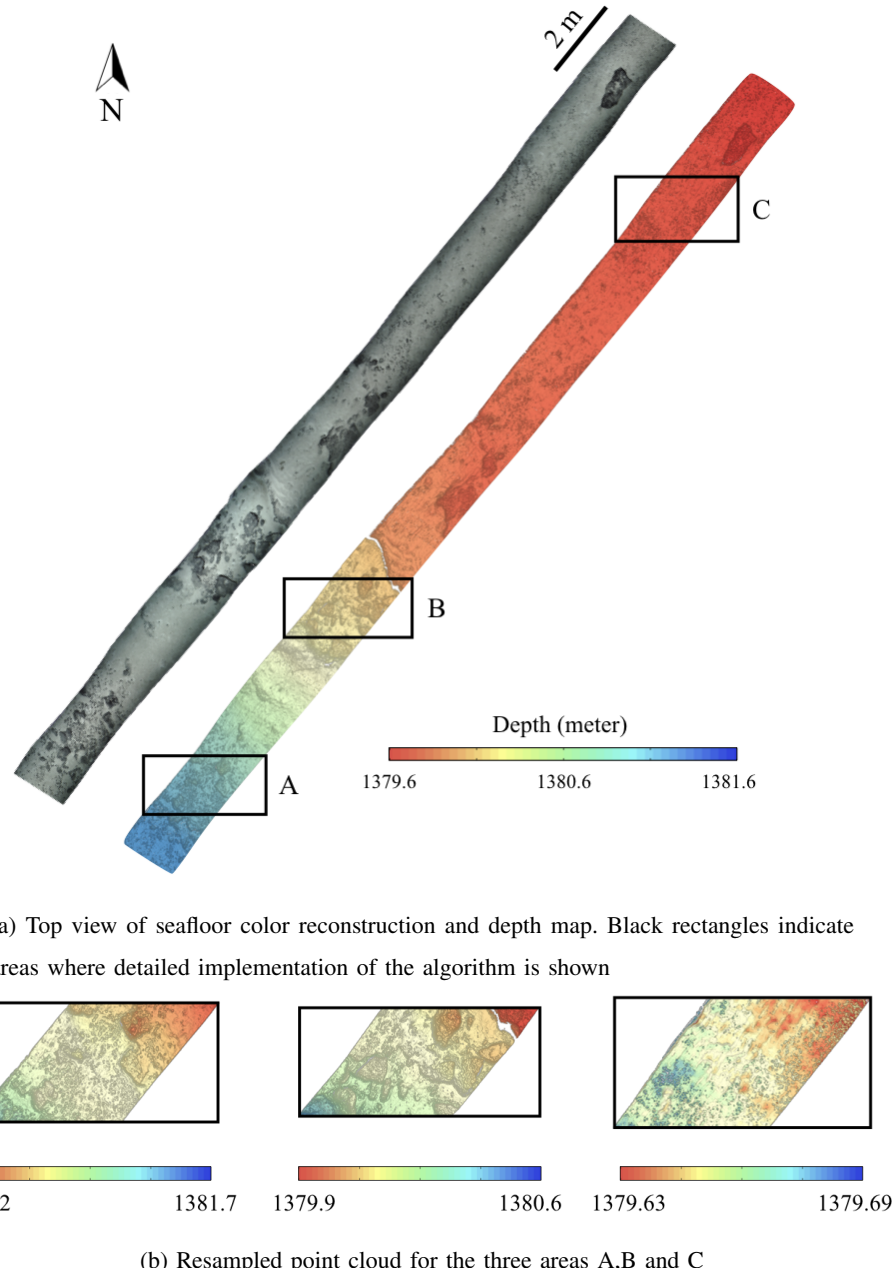


Fig. 4. Seafloor bathymetry mapped using high resolution mapping system

138 The mapping system generates the bathymetry point cloud as northing, easting and depth. The  
 139 point cloud generated from the high resolution mapping system is unstructured and resampled  
 140 to a uniform grid resolution  $g_{res}$ . The points resampled with a resolution of 10 mm are seen in  
 141 Fig. 4b.

142 *B. Landing area detection*

143 Conditions for safe landing on the seafloor are determined to identify landing area in the high  
 144 resolution mapped bathymetry. Landing on sloping surfaces is analyzed for the effects from the  
 145 righting moment of the AUV, ground friction and seafloor currents. Analysis for safe landing on  
 146 objects on the seafloor is made considering their heights. In this work, we propose the design on  
 147 an AUV with negative buoyancy. AUVs are designed and navigate with their centre of buoyancy  
 148  $C_B$  vertically above the centre of gravity  $C_G$ . The key parameters to judge the safety of landing  
 149 are given in Table III and are defined in Fig. 5. The table also shows the parameter values used  
 150 in the simulation of the landing algorithm.

TABLE III  
PHYSICAL PROPERTIES OF UNDERWATER PLATFORM

Property	Description	Value
$l_u$	length of landing AUV	1.7 m
$b_u$	width of landing AUV	0.5 m
$h_u$	height of landing AUV	0.45 m
$F_G$	force of gravity (for 65 Kg mass)	637 N
$F_B$	force of buoyancy (for 62 Kg mass)	608 N
$F_R$	net downward force	29 N
$d_g$	vertical distance to $C_G$	0.25 m
$d_m$	vertical distance between $C_G$ and $C_B$	0.05 m

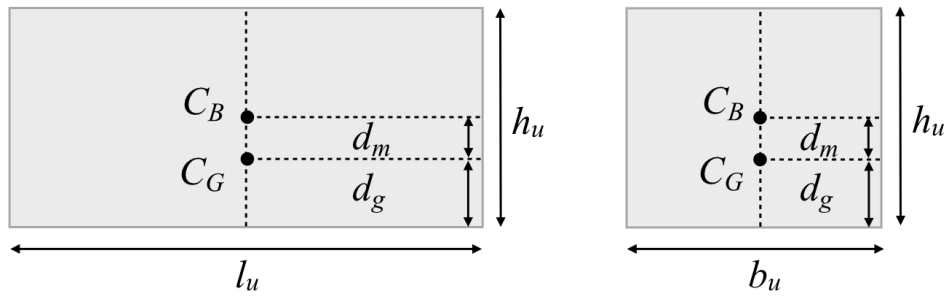


Fig. 5. Side and top view of an AUV with parameters used to determine landing conditions

151 1) *Landing on sloping surface:* When landing on a sloping surface, the AUV is considered  
 152 safe when it can remain stationary and in full contact with the slope. In this work, we determine  
 153 the minimum slope of the surface for the geometry of the AUV where it can meet this condition.

154 The landing of the AUV on surface with slope is analyzed along different landing orientations  
 155 of the AUV  $\psi$  to find this minimum slope  $\theta_c$  as seen in Fig 6. While landing, the AUV first  
 156 makes contact with the slope along its smaller edge  $b_u$  for orientations  $0^\circ$  and  $90^\circ$  and longer  
 157 edge  $l_u$  for orientations  $180^\circ$  and  $270^\circ$ . For all other orientations, the AUV makes contact along  
 158 one of its corners.

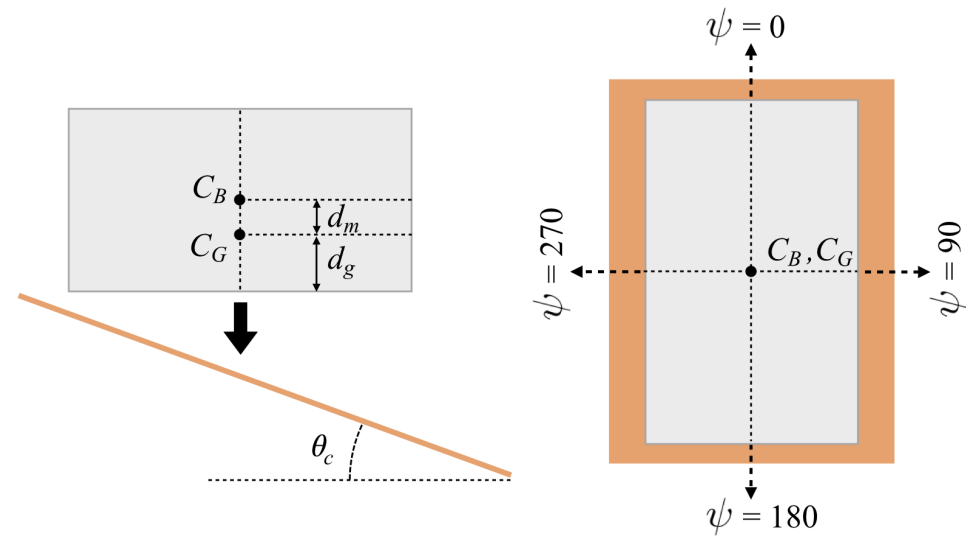


Fig. 6. Side and top view of an AUV landing on a sloping surface

159 After making contact, the AUV can rotate to a maximum angle which is determined by the  
 160 righting moment of the AUV. The AUV rotates along the plane formed by  $C_G$ ,  $C_B$ , point  $P$   
 161 and  $P'$  as seen in Fig 7. For a distance  $d_\psi$  along landing orientation  $\psi$ , the maximum angle of  
 162 rotation is given by the equation:

$$\theta_\psi = \tan^{-1} \left[ \frac{(d_\psi \times F_R)}{(d_m \times F_B) - (d_g \times F_R)} \right] \quad (1)$$

164

165

166 For safe landing, the AUV should make contact with the ground before or at its maximum  
 167 angle of rotation. While landing along its edges or when normal to the diagonal as seen in Fig 7,  
 168 the AUV can make full contact with the surface in one stage. For other orientations, the AUV  
 169 rotates until one of its edges makes contact with the slope after which it rotates about that edge  
 170 to make full contact with the surface. The landing of the AUV was simulated along orientations

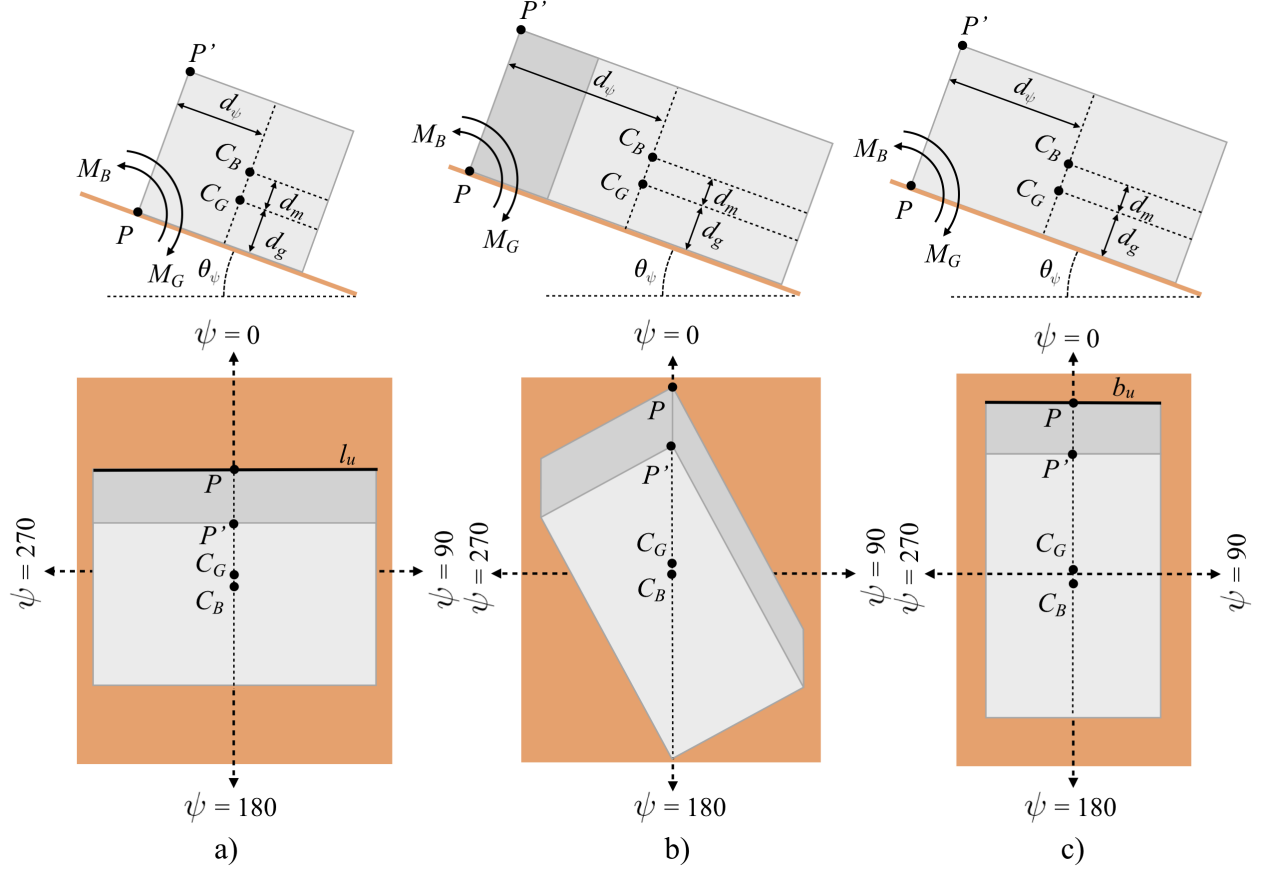


Fig. 7. AUV landing on a sloping surface along different orientations

from  $0^\circ$  to  $360^\circ$  to calculate the slope where the AUV can make full contact with the surface for each orientation as seen in Fig 8. Simulation was also performed for 1, 2 and 4 aspect ratios of  $l_u$  and  $b_u$  to represent different types of underwater AUVs. From these it was determined that minimum rotation occurs when the AUV lands on its shorter edge  $l_u$  as in Fig 7a resulting in the smallest slope of ground where the AUV can land. The minimum slope of the ground where the AUV can land safely  $\theta_c$  is then calculated by using  $d_\psi = 0.5 \times b_u$  in Equation 1 as follows:

$$\theta_c = \tan^{-1} \left[ \frac{(0.5 \times b_u \times F_R)}{(d_m \times F_B) - (d_g \times F_R)} \right] \quad (2)$$

178

179

180 The value of the minimum slope of the ground  $\theta_c$  for the simulation using the dimensions of  
181 the AUV is calculated as  $17.7^\circ$ .

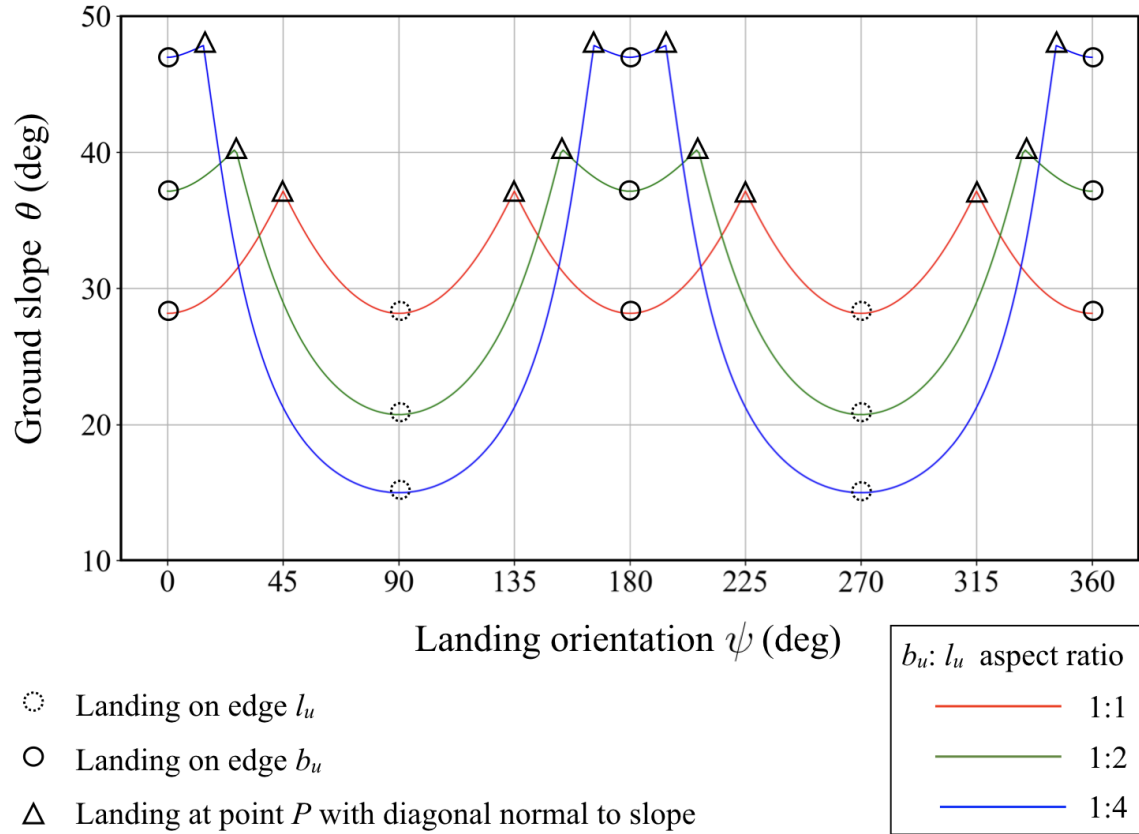


Fig. 8. Slope calculated for different landing orientations and aspect ratios of the AUV

182 Once landed, the AUV can remain stationary on the sloping surface if the force of friction  
 183  $F_F$  counters the component of gravity  $F_G$  along the slope and the force due to seafloor currents  
 184  $F_C$  pushing the vehicle downslope as seen in Fig 9. The slope of the surface where the vehicle  
 185 can remain stationary depends on the coefficient of friction  $\mu$  between the AUV and seafloor.  
 186 The relation between the velocity of seafloor currents  $v$  and the slope at which the vehicle can  
 187 remain stationary without slipping while landing along its longer edge  $l_u$  is calculated. For a  
 188 drag coefficient  $C_d = 1.05$  and density  $\rho = 1000 \text{ Kg/m}^3$ , the velocity of seafloor currents is then  
 189 calculated as:

$$190 \quad F_c = (F_G - F_B) \times (\mu \cos \theta - \sin \theta) \quad (3)$$

$$191 \quad v_c = \sqrt{\frac{2 \times F_c}{C_d \times \rho \times l_u \times h_u}} \quad (4)$$

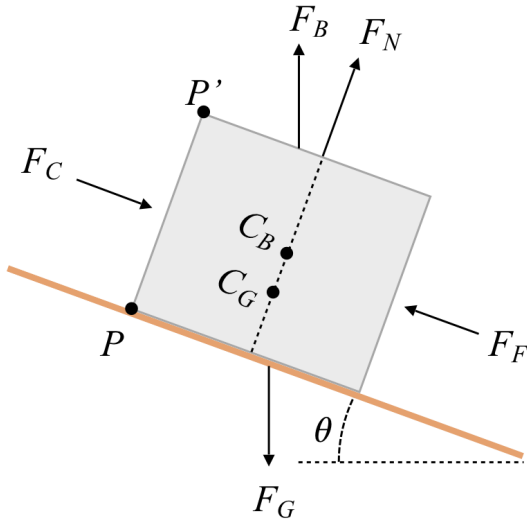


Fig. 9. Forces acting on the AUV after landing on the sloping surface

192 Since the seafloor can have different compositions, it is difficult to estimate the exact coefficient  
 193 of friction without identifying the actual nature of the seafloor. Hence, to analyze the effects of  
 194 friction, current velocity values are calculated for angles between  $0^\circ$  to  $35^\circ$  and coefficients of  
 195 friction 0.1 and 0.6. The values of coefficients of friction are selected based on previous seafloor  
 196 measurements [33] and seafloor currents using the Gebco database. The results indicate that the  
 197 vehicle seafloor current values are within acceptable limits as seen in Fig. 10.

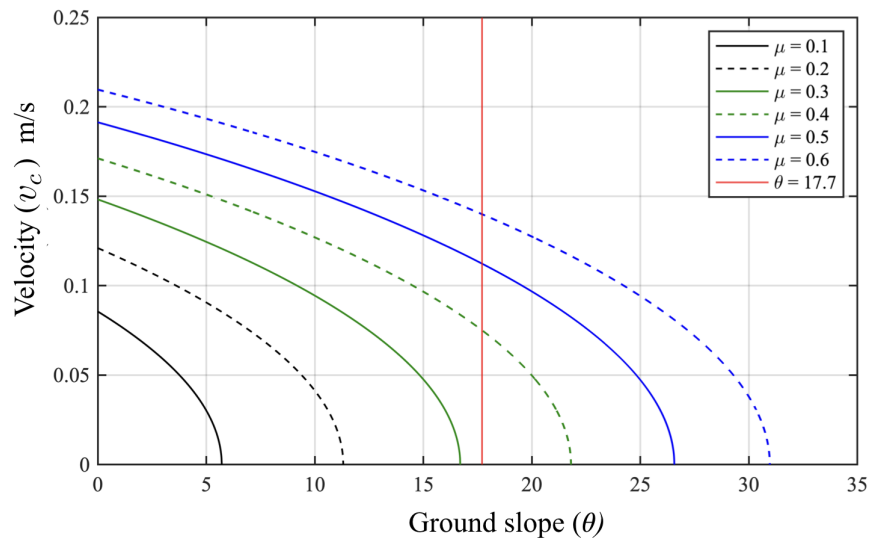


Fig. 10. Analysis of seafloor currents and friction on the ground slope

198 2) *Landing on object on the seafloor*: While landing on objects, the AUV is considered safe  
 199 if the remaining part of the AUV makes full contact with the ground and is stable. Unfavorable  
 200 conditions occur when the vehicle lands on an object and is partially suspended due to its righting  
 201 moment. In this work, we analyze the the landing of an AUV at a point  $P_i$  on the edge on an  
 202 object at a distance  $d_i$  from the  $C_G$  of the AUV as seen in Fig 11a.

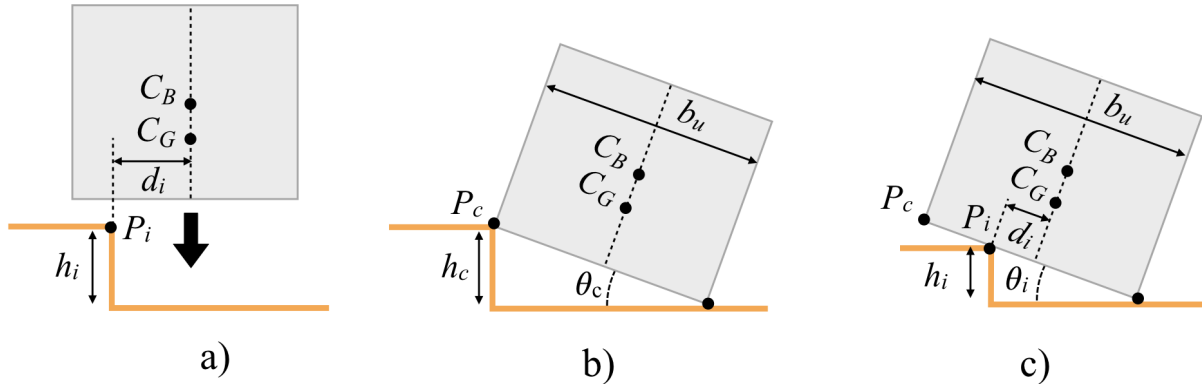


Fig. 11. a) Vehicle landing on an object on the seafloor b) Extreme condition of landing on an object c) Landing at a point between extreme condition and the centre line

203 Extreme condition occurs when the AUV lands along its longer edge  $l_u$  on the object at point  
 204  $P_c$  thereby making the slope  $\theta_c$  with the ground as seen in Fig 11b. The maximum height of the  
 205 object face  $h_c$  where the AUV can land safely is then calculated as:

$$206 \quad h_c = b_u \times \sin \theta_c \quad (5)$$

207 The maximum height of the object face  $h_c$  for our simulation is calculated as 0.152 m. For  
 208 all other points  $P_i$  between  $P_c$  and the  $C_G-C_B$  centre line, we calculate the maximum angle of  
 209 rotation of the AUV after making contact the object using Equation 1 as:

$$210 \quad \theta_i = \tan^{-1} \left[ \frac{(d_i \times F_R)}{(d_m \times F_B) - (d_g \times F_R)} \right] \quad (6)$$

211

212

213 from where we can calculate the maximum height of the object face for distance  $d_i$  as:

$$214 \quad h_i = (0.5 \times b_u + d_i) \times \sin \theta_i \quad (7)$$

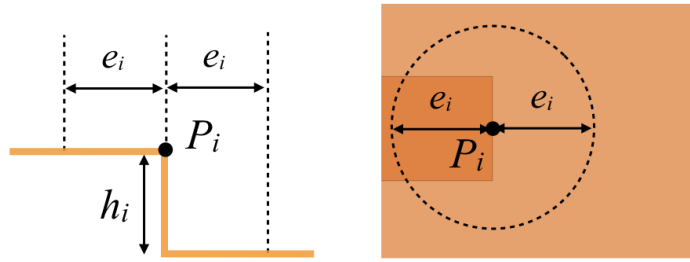


Fig. 12.  $C_G$  exclusion where the centre of gravity of the AUV is prohibited from landing

215 This allows us to create a  $C_G$  exclusion zone  $e_i$  of size  $d_i$  around each face of the object with  
 216 height  $h_i$  where the  $C_G$  of the AUV is prohibited from landing as in Fig 12. The  $C_G$  exclusion  
 217 zone calculated in steps of 5 mm equivalent to the mapping resolution for the dimensions of the  
 218 AUV is seen in Fig 13.

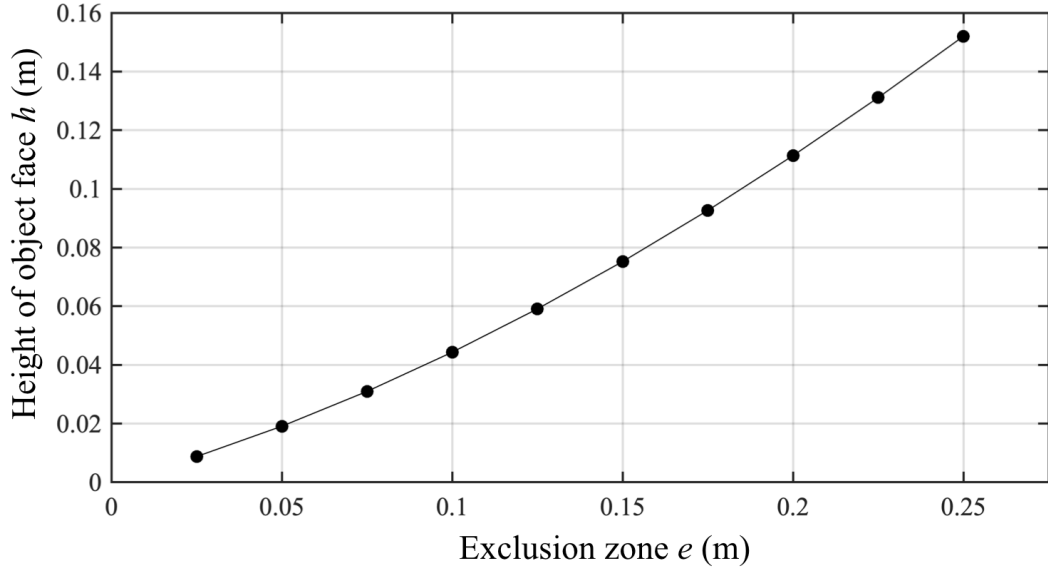


Fig. 13. Exclusion zone for height of objects faces

219 The vehicle should be prohibited from landing on object faces with height more than  $h_c$   
 220 requiring a  $C_G$  exclusion zone of size half the diagonal of the AUV in all directions. However,  
 221 since most AUVs are not circular in shape, the  $C_G$  exclusion zone for these points can be  
 222 calculated based on the geometry of the AUV and the heading during landing  $\alpha$ . This will also  
 223 reduce the size of the  $C_G$  exclusion zone. Using the conditions identified for safe landing, the  
 224 flowchart of the algorithm for landing area and exclusion zone detection is seen in Fig 14.

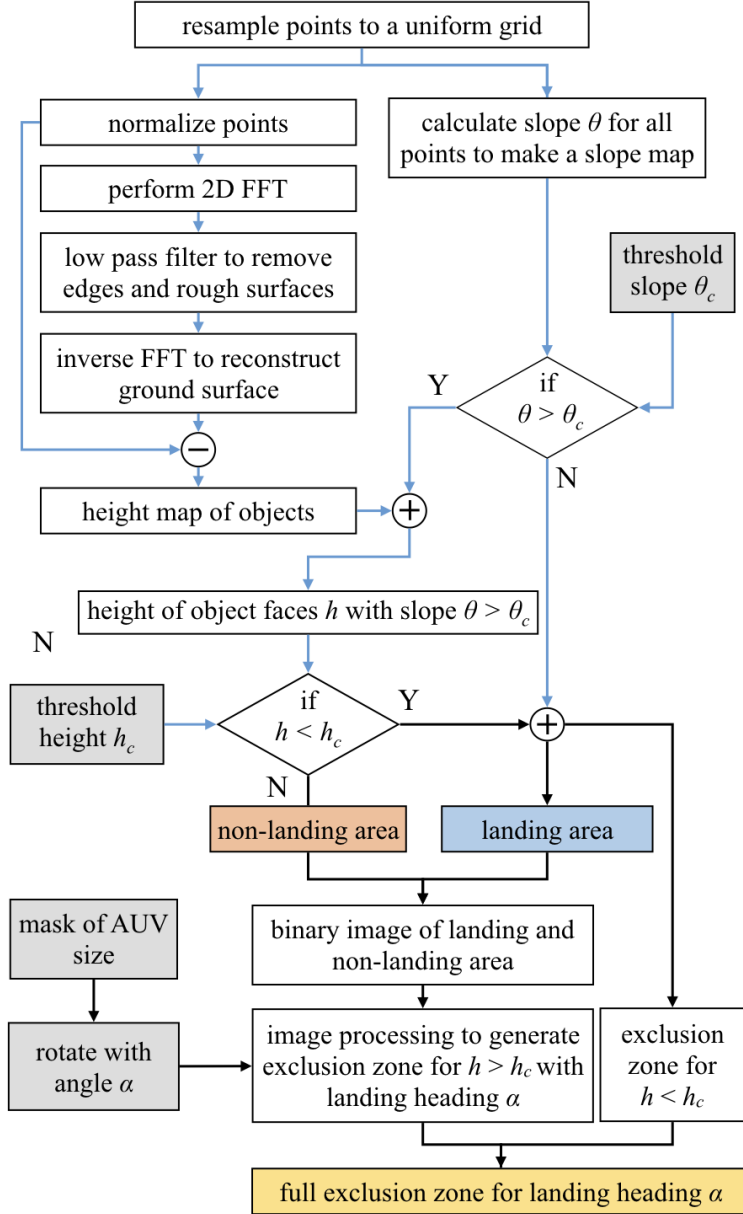


Fig. 14. Flowchart for detection of landing area and generation of  $C_G$  exclusion zone

225 3) Processing point cloud: A slope map is generated for the resampled point cloud. Two  
 226 vectors are computed from three neighboring points making a triangle whose cross product  
 227 is taken to find the normal vector. The angle of this normal vector to the horizontal is then  
 228 calculated as the slope. Slope map generated for the three areas A,B and C is seen in Fig. 15a.  
 229 Slope threshold  $\theta_c$  is applied to the slope map to generate a binary slope threshold map. The  
 230 slope threshold map for  $h_c = 17.7^\circ$  for the simulation is seen in Fig. 15b.

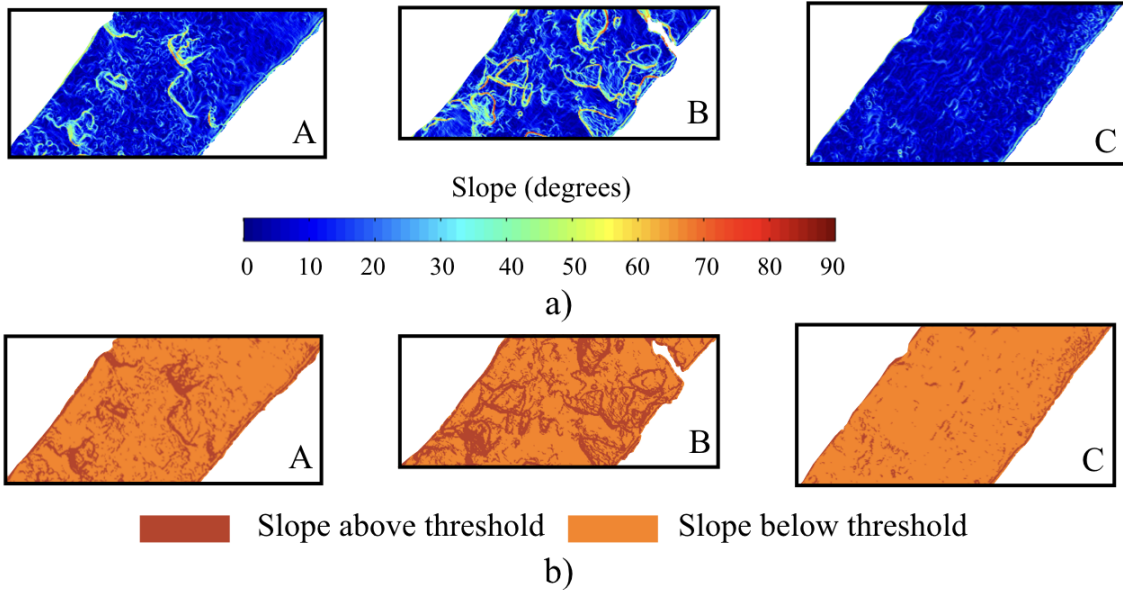


Fig. 15. a) Slope calculated for areas A B and C. Area B shows objects having faces with higher slope than block C and A. Area C shows more smoother surface with less slope b) Slope threshold map for the three areas

231 Laser projections of different seafloor terrain show distinctive profiles. The frequency content  
 232 of these profiles is analyzed for separating objects from the ground surface. Flat areas are  
 233 dominated by low frequency components of the profiles while the high frequency components  
 234 represent the sharp edges of objects and rough surfaces. Analysis is performed on in each area  
 235 using a two dimensional Fast Fourier Transform (FFT). The points in the area are zero filled on  
 236 all sides to form a  $N \times N$  matrix, where  $N$  is the next power of 2 more than the largest dimension  
 237 of the area. The depth values of the points are then normalized to remove the DC component  
 238 by subtracting the mean depth value and rotated along their Eigenvectors. Two dimensional  $N$   
 239 point FFT is performed on the normalized values to convert them to frequency domain values.  
 240 The frequency bins are  $n \times f_s/N$ , where  $n = 1, 2, \dots, N/2$  and  $f_s = 1/g_{res}$  the sampling  
 241 frequency. A low pass filter with a linear phase response with nearly even response in the pass  
 242 band and a sharp cut-off is applied to the frequency domain values to suppress the high frequency  
 243 components. For cut-off frequency  $f_c$ , filter order  $n$  and frequency bins  $f$ , the equation of the  
 244 filter used is:

$$245 \quad h_l(f) = \frac{1}{\sqrt{1 + (\frac{f}{f_c})^{2n}}} \quad (8)$$

246 A filter order of 3 is used to provide suitable sharpness of damping. The filter provides a 3 dB  
 247 attenuation at the cut-off frequency. To decide the cut off frequency we identify the minimum  
 248 size of the object considered as ground. For an object of size  $\sigma$ , represented by a step function,  
 249 the equivalent sync function in frequency domain has first zero crossings at  $2/\sigma$  [34] [35]. The  
 250 cut-off frequency is set as  $f_c = 2/\sigma$  which indicates the frequency represented by the size of the  
 251 object at the sampling resolution.  $f_c = 5$  is used in this work. The filter function is rotated around  
 252 the zero frequency to form a  $N \times N$  point filter and multiplied to the frequency domain values  
 253 element by element. An inverse two dimensional FFT produces smoothed values representing  
 254 the ground surface. The normalized point cloud is compared to the ground surface to generate  
 255 a height map of objects as seen in Fig. 16.

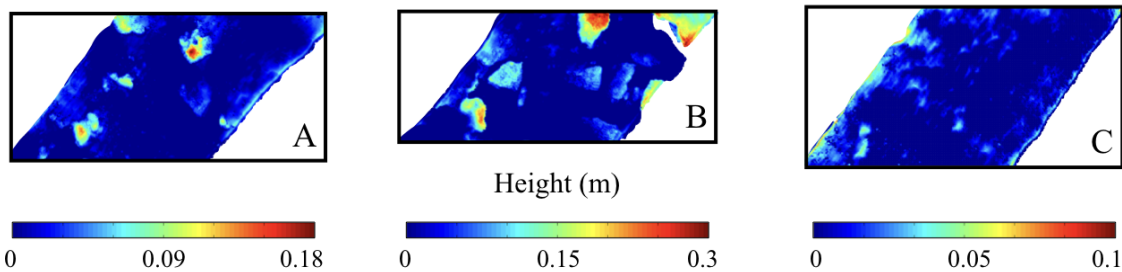


Fig. 16. Height map for areas A B and C. Areas A and B show large objects on the seafloor compared to area C

256 Height of object faces  $h$  is extracted in areas above the slope threshold  $\theta > \theta_c$  from the height  
 257 map of objects as in Fig. 17b. A  $C_G$  exclusion zone is generated for object faces with height  
 258 less than height threshold  $h < h_c$ , using values calculated from Equation 6 and 7 and shown  
 259 in Fig. 13. For this, location of all points having a certain height range are identified to form  
 260 a binary image. Morphological dilation is then performed on this binary image using a circular  
 261 structural element with radius equal to size of the exclusion zone for that height. Object faces  
 262 with height above the threshold  $h > h_c$  are identified to make a binary image with non-landing  
 263 and landing area. Landing area identified for height threshold of 0.152 m is seen in Fig. 18a.  
 264 Since the AUV can land along different headings, the  $C_G$  exclusion zone for object faces above  
 265 height threshold is made taking into account the landing heading  $\alpha$  and the geometry of the  
 266 AUV. For this, a rectangular structural with dimensions in pixels equal to the size of the AUV  
 267 is generated. The structural element is then rotated to the landing heading to generate a new  
 268 structural element representing the rotated AUV.

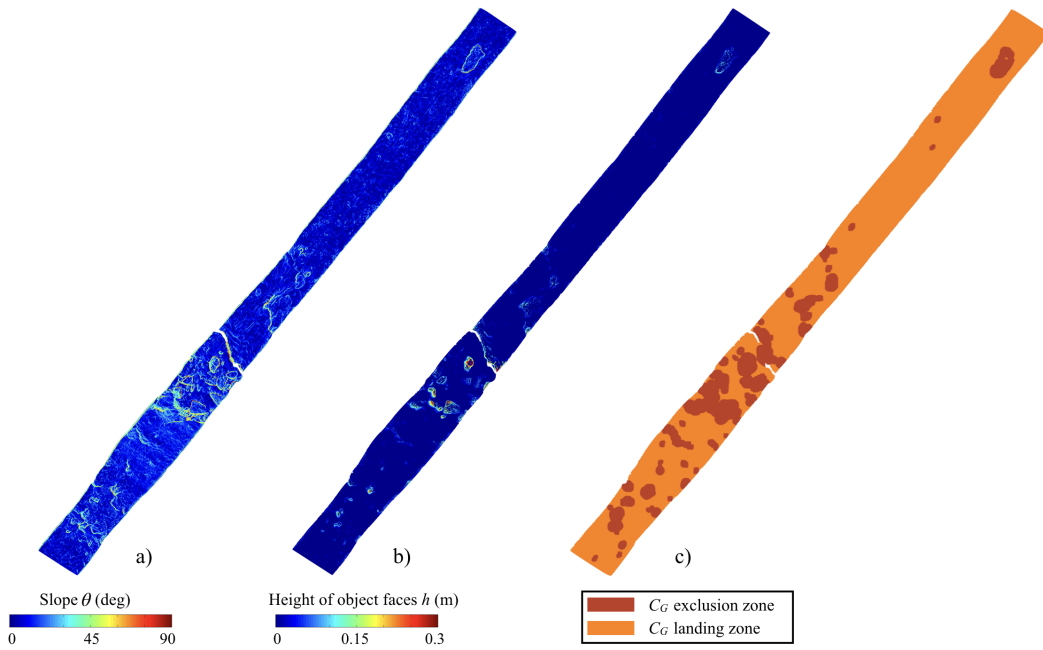


Fig. 17. a) Slope map of the mapped bathymetry b) Height of object faces  $h$  for slope  $\theta > \theta_c$  c)  $C_G$  exclusion zone for object faces  $h < h_c$

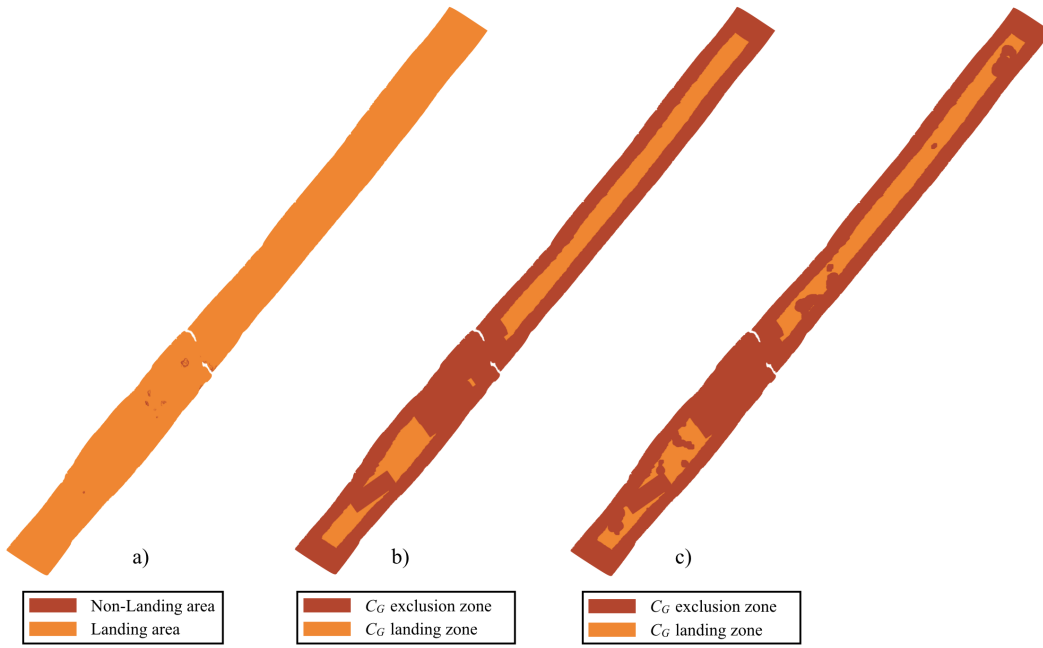


Fig. 18. a) Landing area for height threshold  $h > h_c$  b)  $C_G$  Exclusion zone for landing area with  $55^\circ$  landing heading c) Full  $C_G$  exclusion zone for object faces  $h < h_c$  and landing area with  $55^\circ$  landing heading

269 Image opening is performed between the rotated structural element and the binary image to  
 270 find area where the AUV can fit in the landing area. The points are further eroded using the  
 271 rotated structural element to find area where the  $C_G$  of the AUV can land. The remaining are  
 272 marked as  $C_G$  exclusion zone for the landing heading.  $C_G$  exclusion zone for a landing heading  
 273 of  $55^\circ$  is as seen in Fig 18b. This exclusion zone is then combined with that generated for object  
 274 faces with height less than height threshold  $h < h_c$  to make a full  $C_G$  exclusion zone as seen  
 275 in Fig 18c.

276 *C. Identifying landing sites*

277 Landing sites are identified where the AUV can fit and safely land along a landing heading.  
 278 For each heading, area other than the  $C_G$  exclusion zone,  $C_G$  landing zone is split into grounds  
 279 based on eight neighboring connected pixels. Each group is identified as a landing site. The  
 280 three landing sites identified for the landing heading of  $55^\circ$  can be seen in Fig 19a.

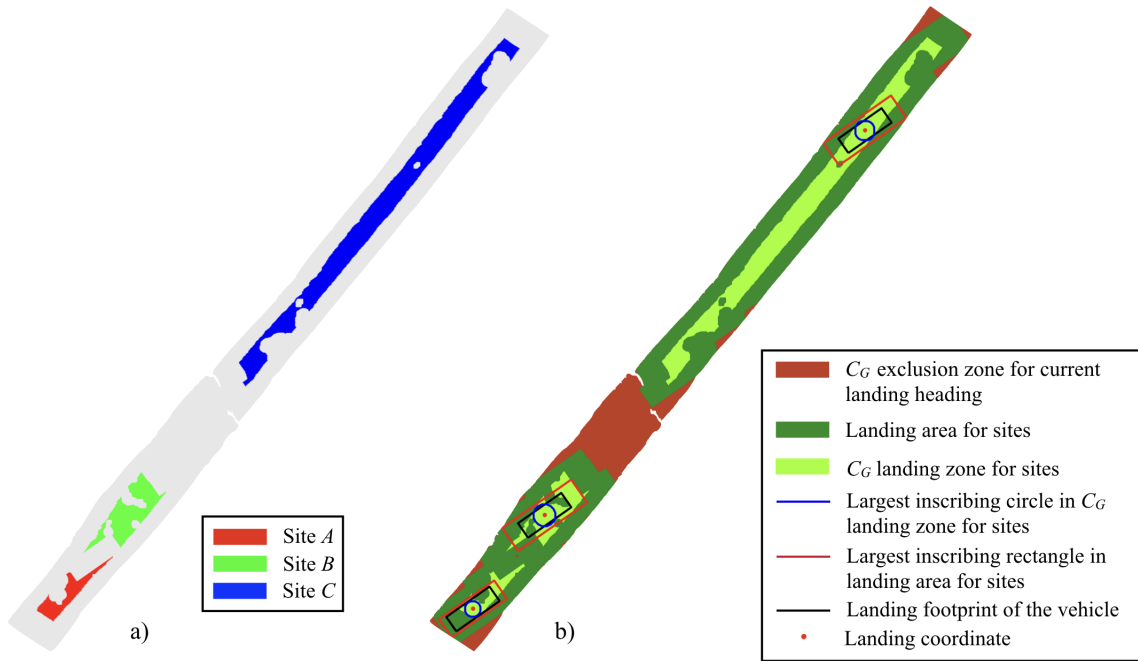


Fig. 19. a) Landing sites identified for  $55^\circ$  landing heading b) Landing point calculation

281 Small groups of points are rejected since they are too small for the AUV to relocate and navigate  
 282 for landing due to positioning errors. A landing coordinate is calculated for each site where the  
 283 AUV can land furthest away from the boundary of the site. For this, the largest circle that can be

284 inscribed in the site is calculated and centre of this circle is taken as the landing coordinate. The  
 285 footprint of the vehicle around the landing coordinate along the landing heading is generated to  
 286 form a rectangle where the properties of the landing site are extracted. The landing coordinates  
 287 calculated for the site along landing heading of  $55^\circ$  are seen in Fig 19b. The following properties  
 288 of the landing site are extracted:

289

290 1) *Site slope  $P_s$* : The mean landing slope  $\bar{\theta}$  is calculated for the points in the landing footprint  
 291 of the AUV. The slope is then normalized using the threshold slope  $\theta_c$  to get the value of  $P_s$ :

$$292 \quad P_s = \frac{\bar{\theta}}{\theta_c} \quad (9)$$

293 2) *Site safety  $P_f$* : A safety factor is calculated for the landing point which indicated how  
 294 far the vehicle is from the edges of the landing site. For each site, the landing area for that  
 295 site is calculated by morphological dilation of the site using the rotated structural element. The  
 296 largest rectangle around the landing coordinate that can be inscribed within this landing area  
 297 having same aspect ratio and landing heading as the vehicle is calculated. The ratio of area of  
 298 this rectangle  $A_r$  to the footprint of the vehicle  $A_f$  is calculated as a safety ratio. Since values  
 299 above a certain limit do not provide any additional safety, the safety ratio is limited to 5. The  
 300 value of  $P_f$  is then calculates as:

$$301 \quad P_f = \frac{1}{4} \left( 5 - \frac{A_r}{A_f} \right) \quad (10)$$

302 3) *Site roughness  $P_r$* : Roughness value  $R$  is calculated for area under the the vehicle footprint  
 303 as the average deviation of the height values  $h$  from the mean  $\bar{h}$ . This value is then normalized by  
 304 comparing with the maximum possible roughness for any terrain under the vehicle footprint  $R_m$ .  
 305 Since the landing coordinate is not included in the  $C_G$  exclusion zone, the worst case scenario  
 306 of the height map is as seen in Fig. 20. The roughness calculated for this is  $R_m = 0.03$ .

$$307 \quad R = \frac{1}{n} \sum_{i=1}^n |h_i - \bar{h}| \quad (11)$$

$$308 \quad P_f = \frac{R}{R_m} \quad (12)$$

309

310

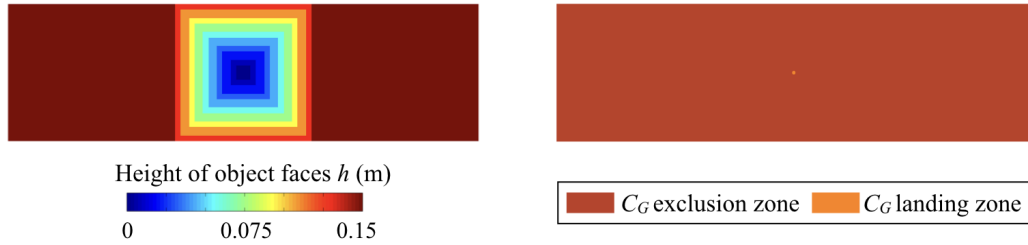


Fig. 20. Area equal to the landing footprint of the vehicle with possible height values with the centre as landing zone

311 Landing cost  $C_s$  is calculated for each site as the average of the three extracted site properties:

312

$$C_s = \frac{1}{3} [P_s + P_f + P_r] \quad (13)$$

313 Landing costs calculated for the three sites for landing heading  $55^\circ$  are seen in Table IV. The  
314 final landing site for this heading is selected as the one with least landing cost, in this case site  
315 C.

TABLE IV  
LANDING SITE PROPERTIES

Site	$P_s$	$P_f$	$P_r$	$C_s$
A	0.54	0.85	0.29	0.56
B	0.67	0.62	0.32	0.54
C	0.34	0.65	0.15	0.38

316 *D. Selecting final landing site*

317 To select a final landing site for the mapped bathymetry, we need to analyze landing sites along  
318 different landing headings. The landing site with the least landing cost can be along any landing  
319 heading depending on the vehicle geometry and the seafloor terrain. Landing sites are identified  
320 for landing headings between  $-90^\circ$  and  $90^\circ$  in steps of  $5^\circ$ . Landing sites along the opposite  
321 headings are identical due to the rectangular nature of the structural element. The landing costs  
322 calculated for all the landing candidates are seen in Fig. 21. The landing site B for landing  
323 heading  $40^\circ$  has the least landing cost and selected as the final landing candidate. The properties  
324 for final landing candidate are as in Table V.

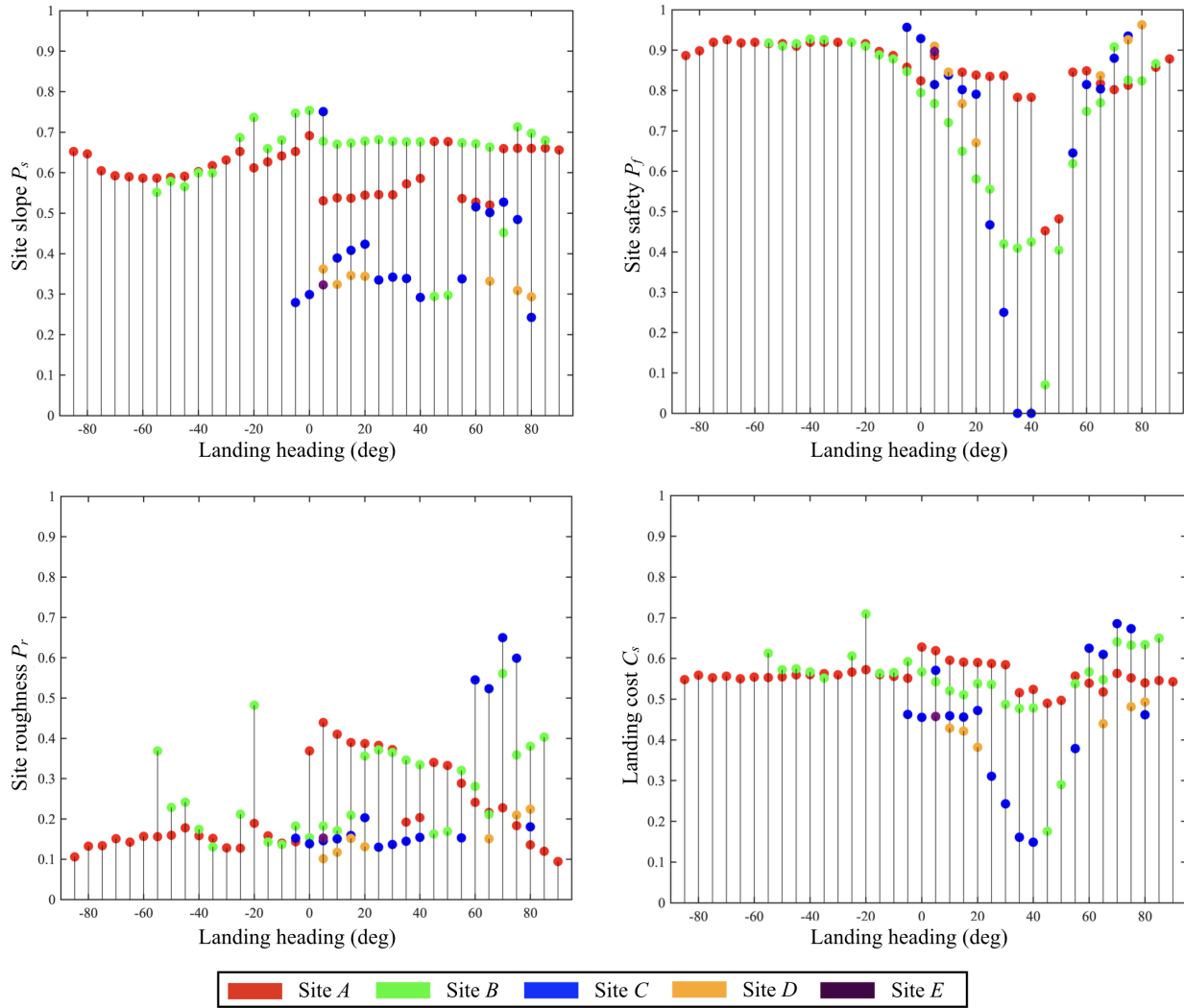


Fig. 21. Properties of the landing sites

TABLE V  
PROPERTIES FOR FINAL LANDING SITE

Property	Value
Landing heading	40° or 220°
Mean depth	1379.72 m
$P_s$	0.29
$P_f$	0.00
$P_r$	0.16
$C_s$	0.15

325

## V. IMPLEMENTATION ON SEAFLOOR DATA

326 The algorithm was implemented on high resolution seafloor bathymetry obtained during the  
 327 survey of a seamount using an equivalent mapping system implemented on an AUV. The ability  
 328 of the algorithm to detect landing sites on different terrain and the landing cost associated with  
 329 it is analyzed.

330 *A. Data collection*

331 Seafloor bathymetry obtained during the KR16-01 research cruise of R/V Keirei, JAMSTEC  
 332 was used for evaluation of the algorithm. Bathymetry was generated along the southern slopes of  
 333 Takuyo No.5 seamount, a large guyot in the Northwest-Pacific. Millimeter order bathymetry was  
 334 generated using a mapping system mounted on the AUV BOSS-A the specifications of which  
 335 are similar to those given in Table. II in Section IV. A 500 m transect along the slope between  
 336 the depths of 1379 m and 1429 m was analyzed in 20 patches of 25 m each as seen in the  
 337 Fig 22.

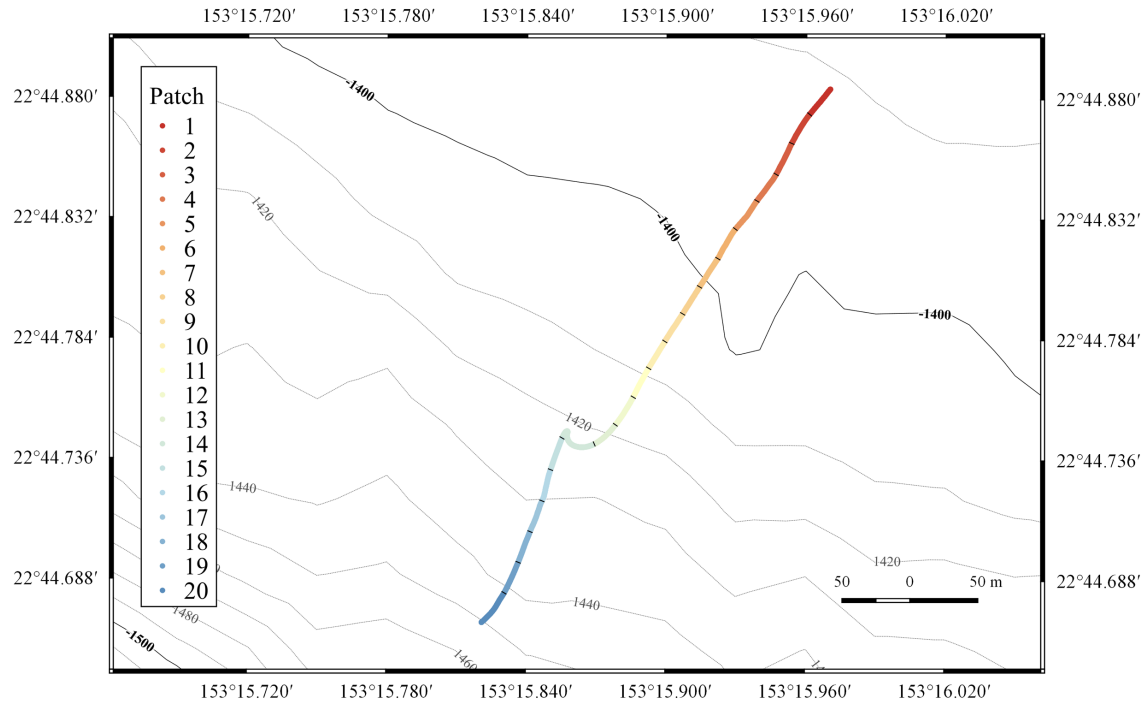


Fig. 22. Vehicle trajectory at No.5 Takuyo seamount where the algorithm is implemented on 20 patches

338 The northern part of the seamount has a more gentle slope while the lower regions contain  
 339 rocky and pillowy outcrops. The number of patches for which the algorithm can successfully

340 detect landing sites is evaluated. The landing cost is analyzed for its relation to the type of  
 341 seafloor terrain.

342 *B. Data analysis and results*

343 The algorithm was implemented on each patch to detect landing sites and select a final landing  
 344 site and heading. The dimensions of the underwater vehicle were kept identical to those used  
 345 for simulation in Section IV, as mentioned in Table III. The other parameters for the landing  
 346 algorithm are identical since the vehicle dimensions used are the same. The algorithm was able  
 347 to detect a landing site in each patch the properties of which can be seen in Fig 23a. The  
 348 landing heading for each patch is close to the mapping heading due to the narrow swath of the  
 349 bathymetry as in Fig 23b.

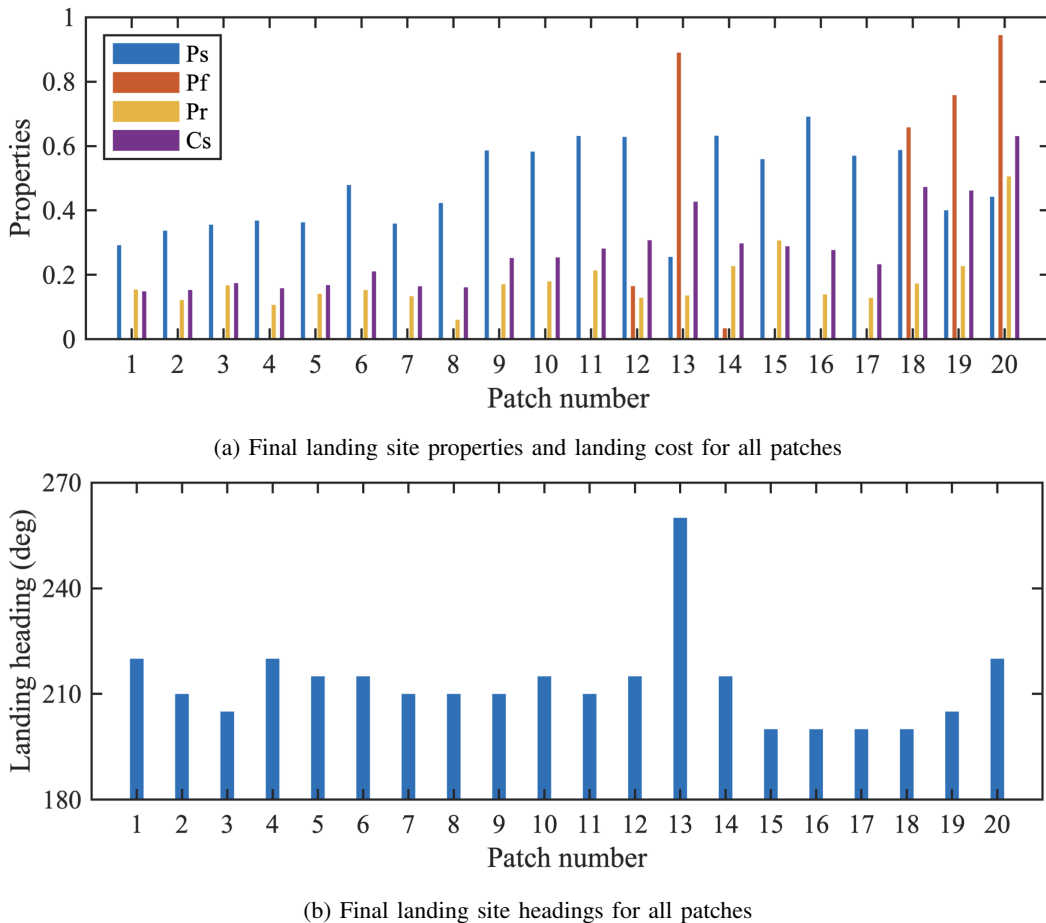


Fig. 23. Results of implementation of landing algorithm on all patches

350 The landing costs for sites towards the south of the transect show higher values due to the  
 351 rough and steep sloping nature of the seafloor as see in Fig 24. The mean  $C_s$  value is found to be

352 0.27. All the sites show high values for Ps due since the mapped bathymetry is along the slope  
 353 of the seamount. Fig 25 shows the final landing sites for three patches along different locations  
 354 in the transect. Patch 1 has the least landing cost due to the wide swath, gently sloping smooth  
 355 surface. Patch 2 shows narrow landing area due to reduced mapping swatch while turning but  
 356 is smooth and gently sloping. Patch 3 towards the lower end of the transect shows extremely  
 357 narrow landing area, rough surface with high slope thereby making the highest landing cost.

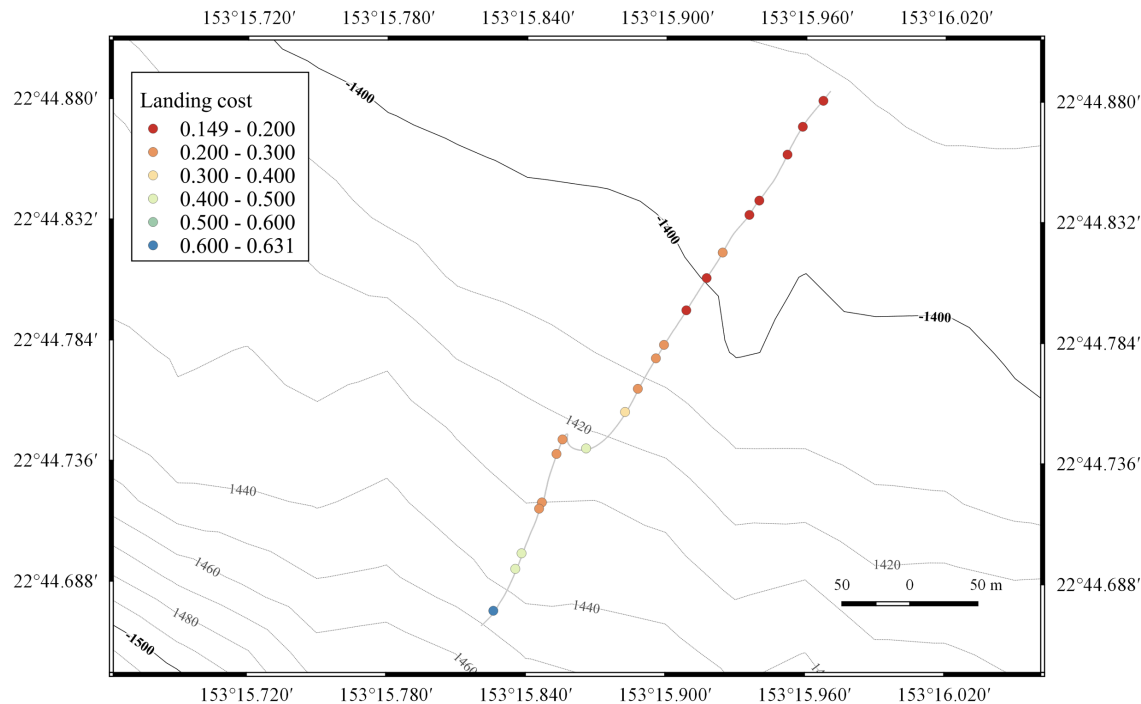


Fig. 24. Landing cost for sites identified

TABLE VI  
RESULTS OF ANALYSIS ON MAPPED BATHYMETRY

Area surveyed	Number of sites	Mean landing cost	Landing cost range	Landing cost Std. Dev.
794.4 sq.m.	754	0.28	0.15 – 0.63	0.13

358

## VI. CONCLUSIONS

359 A framework for intelligent autonomous landing on the seafloor has been proposed and  
 360 developed. The conditions necessary for safe landing were identified, considering the geometry

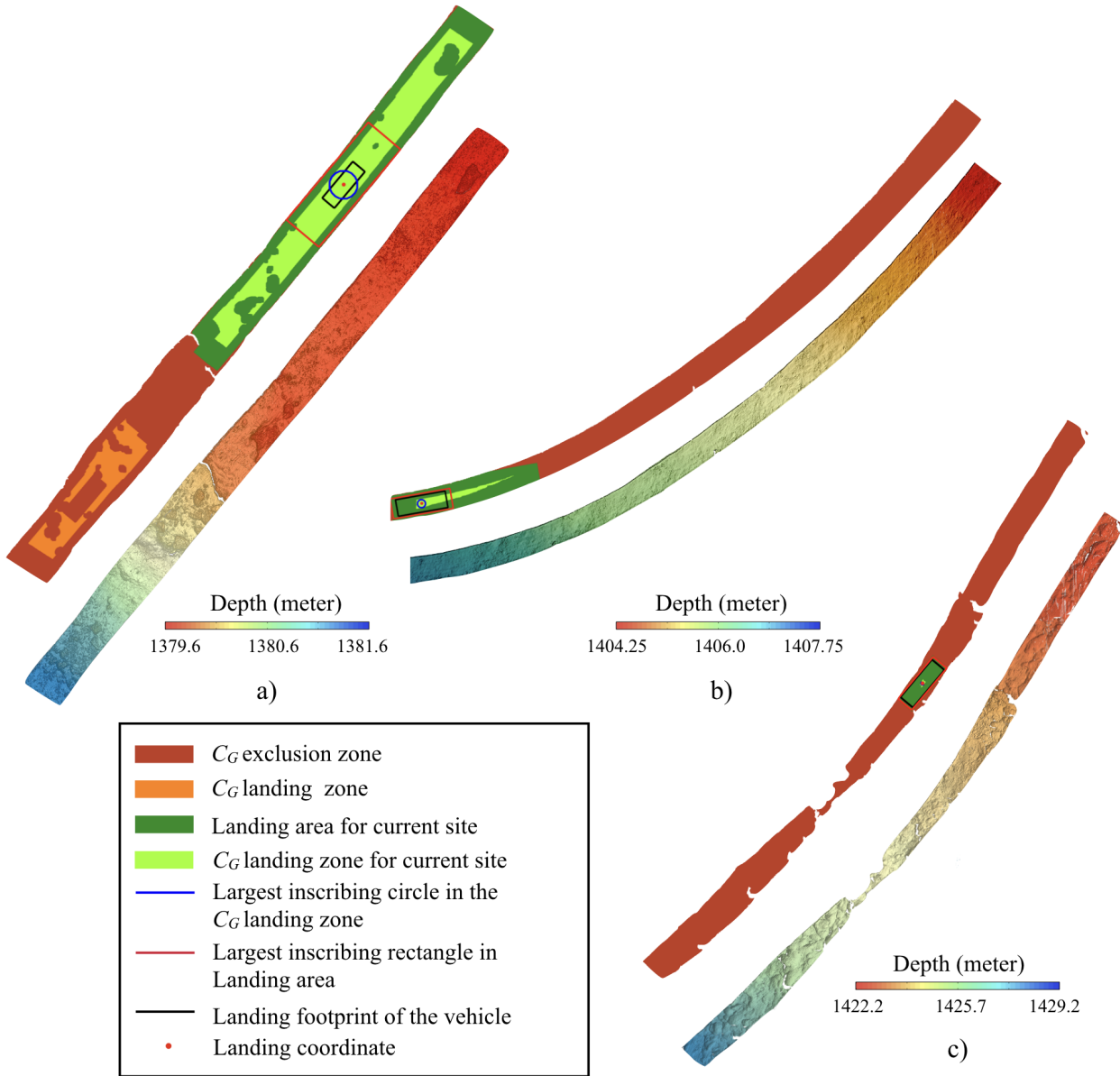


Fig. 25. Landing cost for sites identified

361 of the platform and selecting the optimal landing site based on a cost function. Implementation  
 362 of the landing algorithm was simulated on seafloor data acquired using a similar high resolution  
 363 mapping system. The design of an underwater platform was proposed by identifying the hardware  
 364 required for landing. This work has provided tools for an AUV to perform observations on the  
 365 seafloor with use of in-situ sensors autonomously.

366

## ACKNOWLEDGMENTS

367 The authors would like to thank Y. Nishida of Kyushu Institute of Technology, K. Nagano of  
368 Mitsui Engineering and Shipbuilding, U. Neettiyath of The University of Tokyo and T. Koike  
369 of Kaiyo Engineering for their help in deployment of BOSS-A during the NT15-03 cruise of  
370 R/V Natsushima. We also acknowledge T. Nakatani, now of JAMSTEC and T. Sakamaki of The  
371 University of Tokyo for their valuable assistance and guidance during the experiments. This work  
372 was funded under the Program for the Development of Fundamental Tools for the Utilization of  
373 Marine Resources of the Japanese Ministry of Education.

374

## REFERENCES

- 375 [1] K. Suzuki, J.-i. Ishibashi, Y. Kato, and T. Nozaki, "Preface: Front edge of submarine mineral resources research in Japan,"  
376 *Geochemical Journal*, vol. 49, no. 6, pp. 575–577, 2015.
- 377 [2] A. Usui, K. Nishi, H. Sato, Y. Nakasato, B. Thornton, T. Kashiwabara, A. Tokumaru, A. Sakaguchi, K. Yamaoka, S. Kato,  
378 S. Nitahara, K. Suzuki, K. Iijima, and T. Urabe, "Continuous growth of hydrogenetic ferromanganese crusts since 17 Myr  
379 ago on Takuyo-Daigo Seamount, NW Pacific, at water depths of 800 to 5500 m," *Ore Geology Reviews*, vol. 87, pp. 71–87,  
380 jul 2017.
- 381 [3] T. Schoening, T. Kuhn, D. O. Jones, E. Simon-Lledo, and T. W. Nattkemper, "Fully automated image segmentation for  
382 benthic resource assessment of poly-metallic nodules," *Methods in Oceanography*, vol. 15, pp. 78–89, 2016.
- 383 [4] B. Thornton, A. Bodenmann, O. Pizarro, S. B. Williams, A. Friedman, R. Nakajima, K. Takai, K. Motoki, T. o. Watsuji,  
384 H. Hirayama, Y. Matsui, H. Watanabe, and T. Ura, "Biometric assessment of deep-sea vent megabenthic communities  
385 using multi-resolution 3D image reconstructions," *Deep-Sea Research Part I: Oceanographic Research Papers*, vol. 116,  
386 pp. 200–219, 2016.
- 387 [5] C. De Moustier and H. Matsumoto, "Seafloor acoustic remote sensing with multibeam echo-sounders and bathymetric  
388 sidescan sonar systems," *Marine Geophysical Researches*, vol. 15, no. 1, pp. 27–42, 1993.
- 389 [6] C. Roman, G. Inglis, and J. Rutter, "Application of structured light imaging for high resolution mapping of underwater  
390 archaeological sites," in *OCEANS 2010 IEEE - Sydney*, 2010, pp. 1–9.
- 391 [7] O. Pizarro, S. B. Williams, and J. Colquhoun, "Topic-based habitat classification using visual data," in *OCEANS 2009-*  
392 *EUROPE*. IEEE, May 2009, pp. 1–8.
- 393 [8] T. Maki, A. Kume, T. Ura, T. Sakamaki, and H. Suzuki, "Autonomous detection and volume determination of tubeworm  
394 colonies from underwater robotic surveys," in *OCEANS 2010 IEEE - Sydney*, vol. d. Ieee, May 2010, pp. 1–8.
- 395 [9] T. Takahashi, B. Thornton, K. Ohki, and T. Sakka, "Calibration-free analysis of immersed brass alloys using long-  
396 ns-duration pulse laser-induced breakdown spectroscopy with and without correction for nonstoichiometric ablation,"  
397 *Spectrochimica Acta Part B: Atomic Spectroscopy*, vol. 111, pp. 8–14, sep 2015.
- 398 [10] D. White and H. Dingle, "The mechanism of steady friction between seabed pipelines and clay soils," *Géotechnique*,  
399 vol. 61, no. 12, pp. 1035–1041, 2011.
- 400 [11] D. M. Rubin, H. Chezar, J. N. Harney, D. J. Topping, T. S. Melis, and C. R. Sherwood, "Underwater microscope for  
401 measuring spatial and temporal changes in bed-sediment grain size," *Sedimentary Geology*, vol. 202, no. 3, pp. 402–408,  
402 2007.

- 403 [12] B. Thornton, S. Ohnishi, T. Ura, N. Odano, S. Sasaki, T. Fujita, T. Watanabe, K. Nakata, T. Ono, and D. Ambe, "Distribution  
404 of local  $^{137}\text{Cs}$  anomalies on the seafloor near the Fukushima Dai-ichi Nuclear Power Plant," *Marine Pollution Bulletin*,  
405 vol. 74, no. 1, pp. 344–350, 2013.
- 406 [13] B. Thornton, S. Ohnishi, T. Ura, N. Odano, and T. Fujita, "Continuous measurement of radionuclide distribution off  
407 Fukushima using a towed sea-bed gamma ray spectrometer," 2013.
- 408 [14] B. Thornton, T. Takahashi, T. Sato, T. Sakka, A. Tamura, A. Matsumoto, T. Nozaki, T. Ohki, and K. Ohki, "Development  
409 of a deep-sea laser-induced breakdown spectrometer for in situ multi-element chemical analysis," *Deep Sea Research Part  
410 I: Oceanographic Research Papers*, vol. 95, pp. 20 – 36, 2015.
- 411 [15] M. Saeki, A. Iwanade, C. Ito, I. Wakaida, B. Thornton, T. Sakka, and H. Ohba, "Development of a fiber-coupled laser-  
412 induced breakdown spectroscopy instrument for analysis of underwater debris in a nuclear reactor core," *Journal of Nuclear  
413 Science and Technology*, vol. 51, no. 7-8, pp. 930–938, 2014.
- 414 [16] P. G. Brewer, G. Malby, J. D. Pasteris, S. N. White, E. T. Peltzer, B. Wopenka, J. Freeman, and M. O. Brown, "Development  
415 of a laser raman spectrometer for deep-ocean science," *Deep Sea Research Part I: Oceanographic Research Papers*, vol. 51,  
416 no. 5, pp. 739 – 753, 2004.
- 417 [17] J. Pasteris, B. Wopenka, J. J. Freeman, G. P. Brewer, N. S. White, T. E. Peltzer, and E. G. Malby, "Raman Spectroscopy  
418 in the Deep Ocean: Successes and Challenges," *Appl. Spectrosc.*, vol. 58, pp. 195A–208A, 2004.
- 419 [18] S. A. Stanier, D. J. White, S. Chatterjee, P. Brunning, and M. F. Randolph, "A tool for ROV-based seabed friction  
420 measurement," *Physics Procedia*, vol. 50, pp. 155–162, 2015.
- 421 [19] B. Thornton, A. Asada, A. Bodenmann, M. Sangekar, and T. Ura, "Instruments and Methods for Acoustic and Visual  
422 Survey of Manganese Crusts," *IEEE Journal of Oceanic Engineering*, vol. 38, no. 1, pp. 186–203, jan 2013.
- 423 [20] I. Masmitja, O. Pallares, S. Gomariz, J. Del Rio, T. O'Reilly, and B. Kieft, "Range-only underwater target localization:  
424 Error characterization," *21st IMEKO TC-4 International Symposium on Understanding the World through Electrical and  
425 Electronic Measurement, and 19th International Workshop on ADC Modelling and Testing*, pp. 267–271, 2016.
- 426 [21] G. Inglis, C. Smart, I. Vaughn, and C. Roman, "A pipeline for structured light bathymetric mapping," in *2012 IEEE/RSJ  
427 International Conference on Intelligent Robots and Systems*. IEEE, 2012, pp. 4425–4432.
- 428 [22] Y. Nishida, K. Nagahashi, T. Sato, A. Bodenmann, B. Thornton, A. Asada, and T. Ura, "Autonomous underwater vehicle  
429 boss-a for acoustic and visual survey of manganese crusts," *Journal of Robotics and Mechatronics*, vol. 28, no. 1, pp.  
430 91–94, 2016.
- 431 [23] V. Desaraju and N. Michael, "Vision-based Landing Site Evaluation and Trajectory Generation Toward Rooftop Landing,"  
432 *Rss*, 2014.
- 433 [24] C. S. Sharp, O. Shakernia, and S. S. Sastry, "A vision system for landing an unmanned aerial vehicle," in *Proceedings 2001  
434 ICRA. IEEE International Conference on Robotics and Automation (Cat. No.01CH37164)*, vol. 2, 2001, pp. 1720–1727  
435 vol.2.
- 436 [25] S. Wang, H. Zhang, W. Hou, J. Liang, P. Taylor, H. Zhangy, W. Houy, and J. Liangz, "Control and navigation of the variable  
437 buoyancy AUV for underwater landing and takeoff," *International Journal of Control*, vol. 80, no. 7, pp. 1018–1026, 2007.
- 438 [26] B. Du, Y. Jiang, and H. Zhang, "Dynamic analysis of landing autonomous underwater vehicle," *Transactions of Tianjin  
439 University*, vol. 18, no. 4, pp. 298–304, Aug. 2012.
- 440 [27] B. Douillard, N. Nourani-Vatani, M. Johnson-Roberson, S. Williams, C. Roman, O. Pizarro, I. Vaughn, and G. Inglis,  
441 "FFT-based Terrain Segmentation for Underwater Mapping," in *Proceedings of Robotics: Science and Systems*, Sydney,  
442 Australia, 2012.
- 443 [28] B. Douillard, N. Nourani-Vatani, M. Johnson-Roberson, O. Pizarro, S. Williams, C. Roman, and I. Vaughn, "Frequency-  
444 based underwater terrain segmentation," *Autonomous Robots*, vol. 35, no. 4, pp. 255–269, Jul. 2013.

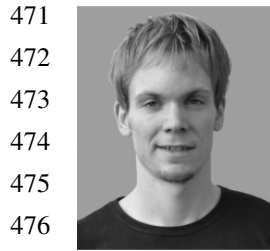
- 445 [29] S. H. Bhandari and S. M. Deshpande, "Feature Extraction for Surface Classification - An approach with Wavelets,"  
446 *International Journal of Computer and Information Science and Engine*, vol. 1, no. 4, pp. 322–326, 2007.
- 447 [30] M. N. Sangekar, B. Thornton, T. Nakatani, and T. Ura, "Development of a landing algorithm for autonomous underwater  
448 vehicles using laser profiling," in *OCEANS'10 IEEE SYDNEY*. Sydney, Australia: IEEE, may 2010, pp. 1–7.
- 449 [31] "Design and Development of Low Cost Variable Buoyancy System for the Soft Grounding of Autonomous Underwater  
450 Vehicles," *2006 IEEE International Conference on Control Applications*, vol. 3, no. 3, pp. 1072–1082, 2008.
- 451 [32] A. Bodenmann, B. Thornton, and T. Ura, "Generation of High-resolution Three-dimensional Reconstructions of the Seafloor  
452 in Color using a Single Camera and Structured Light," *Journal of Field Robotics*, vol. 00, no. 00, pp. 1–19, 2016.
- 453 [33] K. F. Lambrakos, "Marine pipeline soil friction coefficients from in-situ testing," *Ocean Engineering*, vol. 12, no. 2, pp.  
454 131–150, 1985.
- 455 [34] Lyons Richard G., *Understanding digital signal processing*. Addison Wesley Pub. Co Reading, Mass, 1997.
- 456 [35] E. Kalogerakis, A. Hertzmann, and K. Singh, "Learning 3D mesh segmentation and labeling," *ACM Transactions on  
457 Graphics*, vol. 29, no. 4, p. 1, 2010.



563 **Sangekar Mehul Naresh** (M10) received the M.Sc. degree in underwater robotics and Ph.D. degree in  
564 ocean technology from The University of Tokyo, Japan, in 2010 and 2014, respectively. He is working  
565 at present as a project researcher at the Thornton Lab, Institute of Industrial Science, The University  
566 of Tokyo. Currently, he works on techniques for intelligent, multi-layer resolution mapping of the seafloor  
567 using autonomous underwater vehicles. He is also working on developing algorithms for analysis of high  
568 resolution seafloor bathymetry and correlating it with other measured seafloor parameters.



784 **Thornton Blair** (M07) received the B.Eng. degree in ship science and the Ph.D. degree in underwater  
785 robotics from The University of Southampton, Southampton, U.K., in 2002 and 2006, respectively. He is  
786 at present an Associate Professor at the the University of Southampton and also affiliated with the Ocean  
787 Perception Laboratory, Institute of Industrial Science, The University of Tokyo. His research interests  
788 involve the development of in-situ sensors and data processing techniques for integrated acoustic, visual,  
789 and chemical survey of marine minerals and environment monitoring. He is dedicated to fielding real  
790 systems in real environments and overcoming bottlenecks in the flow of information from data collection to human interpretation.



471      **Adrian Bodenmann** (M09) received the M.Sc. degree in microengineering from the Ecole Poly- technique  
472      Fdrale de Lausanne (EPFL), Lausanne, Switzerland, in 2009. He is a Project Researcher at the Underwater  
473      Technology Research Center, University of Tokyo, Tokyo, Japan. Currently, he works on 3-D seafloor  
474      visual mapping and automated data processing algorithms, and is developing a long-range 3-D color  
475      mapping system for wide area marine surveys.  
476



477      **Ura Tamaki** (M91SM02F07) graduated from the Faculty of Engineering, The University of Tokyo, Japan,  
478      in 1972 and received the degree of Doctor of Engineering from the same university in 1977. He is at present  
479      the Professor emeritus of The University of Tokyo and Director, Distinguished Professor of Center for  
480      Socio-Robotic Synthesis, Kyushu Institute of Technology, and Director of Underwater Technology Center  
481      of National Maritime Research Institute. He has developed various types of Autonomous Underwater  
482      Vehicles (AUVs) and related application technologies including navigation methods, a new sensing method  
483      using a chemical sensor, precise seafloor mapping methods, a precise seabed positioning system with a resolution of a few  
484      centimeters, a new sensing system of the thickness of cobalt-rich crust, etc. Finally, he exemplified using these technologies that  
485      AUVs are practicable and valuable tools for deep-sea exploration.